Coarsening of solid β-Sn particles in liquid Pb-Sn alloys: Reinterpretation of experimental data in the framework of trans-interface-diffusion-controlled coarsening

James F. Hickman,[1] Yuri Mishin,[2] Vidvuds Ozoliņš,[3] and Alan J. Ardell[4,*]

[1]*Materials Science and Engineering Division, National Institute of Standards and Technology (NIST), Gaithersburg, Maryland 20899-8910, USA*

[2]*Department of Physics and Astronomy, George Mason University, Fairfax, Virginia 22030-4444, USA*

[3]*Department of Applied Physics, Energy Sciences Institute, Yale University, New Haven, Connecticut 06511, USA*

[4]*Department of Materials Science and Engineering, UCLA Samueli School of Engineering, Los Angeles, California 90095-1595, USA*

(Received 2 February 2021; accepted 16 March 2021; published 1 April 2021)

Previously published data, not ours, on the coarsening of solid β-Sn particles in a liquid Pb-Sn matrix of near-eutectic composition are reanalyzed within the framework of the trans-interface-diffusion-controlled (TIDC) theory of coarsening. The data were obtained under conditions of microgravity from specimens heat-treated at 458 K and containing four equilibrium volume fractions f_e equaling 0.10, 0.15, 0.20, and 0.30. We show that the rate constants $k(f_e)$ in the traditional coarsening equation $\langle r\rangle^3 \approx k(f_e)t$ for the kinetics of growth of the average particle radius $\langle r\rangle$ are nearly independent of f_e, in disagreement with numerous theories wherein coarsening is controlled by diffusion in the host matrix phase. Atom transport in TIDC coarsening is instead controlled by slow diffusion through the diffuse interface, of width δ, separating the dispersed particles from the matrix; the kinetics of this process is independent of f_e. Atomistic simulations were performed to estimate the properties of the solid-liquid (S-L) interface at 458 K, 2 K above the Pb-Sn eutectic temperature. The S-L interfaces normal to (001) and (010) of tetragonal β-Sn were examined and found to have nearly identical properties, including interface widths of $\sim$1.7 nm. In conjunction with the diffusivities in solid β-Sn and liquid hypereutectic Pb-Sn at 458 K, we estimate that TIDC coarsening should prevail for solid Sn particles $<\sim$1700 μm in radius, far exceeding the maximum radius of $\sim$100 μm measured experimentally. The TIDC theory also predicts that the kinetics of growth obeys the equation $\langle r\rangle^n \propto t$. The temporal exponent n was evaluated to be $\sim$2.5, as ascertained by analyzing data on the particle size distributions (PSDs; histograms) for the alloys with $f_e = 0.15$, 0.20, and 0.30. The histograms were converted to experimental cumulative distribution functions (ECDFs) and analyzed using the Kolmogorov-Smirnov (K-S) test applied to the theoretical CDFs predicted by the TIDC theory. We report the first successful application of the K-S test to experimental PSDs concomitant with particle coarsening. From every aspect of the experimental data amenable to analysis, we conclude that the coarsening behavior of solid Sn particles in liquid hypereutectic Pb-Sn alloys is fully consistent with the predictions of the TIDC theory of coarsening.

DOI: 10.1103/PhysRevMaterials.5.043401

I. INTRODUCTION

A polydisperse array of particles situated in a host matrix is inherently unstable because the system can lower its energy by transporting matter from small to large particles, thereby reducing its interfacial area, hence its energy, per unit volume. This is exactly what occurs during particle coarsening (Ostwald ripening). When exposed to temperatures high enough to facilitate the transport of atoms or molecules from the smaller (shrinking) particles in the array to the larger (growing) ones, the kinetics of coarsening becomes measurable, enabling the testing of various theories of this process. Coarsening is an important phenomenon because it affects the stability of material microstructures (especially but not uniquely metallurgical), hence their properties, at high temperatures. It is therefore important in the design and performance of materials used in elevated temperature applications, turbine-blade alloys in jet engines being a familiar example.

Theories of coarsening predict the growth of the average particle radius $\langle r\rangle$ as a function of time t, the kinetics of solute depletion in the host matrix, the kinetics of particle evanescence (the decrease with t of the number of particles per unit volume N_v), and the increase with t of the volume fraction f as the system approaches thermodynamic equilibrium. Because the array of particles is polydisperse, predicting the particle size distribution (PSD) is another theoretical objective.

In the seminal treatises of Lifshitz and Slyozov [1] and Wagner [2] (the LSW theory), the dispersion is infinitely dilute, and the kinetics is controlled by solute diffusion in the matrix [matrix-diffusion control (MDC)]. The LSW theory predicts the well-known result

$$\langle r\rangle^3 - \langle r_0\rangle^3 = kt, \tag{1}$$

where $\langle r_0\rangle$ is the average radius of the assumed spherical particles at the onset of coarsening, measured at $t = 0$, and k is a rate constant that depends on parameters incorporating the thermodynamics and kinetics of the system. Wagner [2] also considered the special case of particle growth controlled

*aardell@ucla.edu

not by diffusion, but instead by an unspecified reaction at the particle-matrix interface [interface reaction control (IRC)]. In that situation, the temporal exponent changes from 3 to 2, and the equation governing the growth of the average radius becomes

$$\langle r\rangle^2 - \langle r_0\rangle^2 = k_I t, \tag{2}$$

where k_I is a rate constant that differs from k and involves parameter(s) associated with the interface reaction.

In MDC coarsening the kinetics of solute depletion of the matrix phase is governed by the equation

$$X - X_e \approx (\kappa t)^{-1/3}, \tag{3}$$

where X is the concentration of solute in the majority matrix phase, X_e is the value of X at thermodynamic equilibrium, and κ is a rate constant that includes the same thermodynamic and kinetic parameters as k in Eq. (1). Equation (3) is expected to be valid at long aging times, when $\langle r\rangle \gg \langle r_0\rangle$ and $\langle r\rangle \approx (kt)^{1/3}$ from Eq. (1).

During MDC coarsening, the volume fraction f increases with aging time according to the equation

$$f \approx f_e - \frac{(\kappa t)^{-1/3}}{\Delta X_e}, \tag{4}$$

where ΔX_e represents the difference between the equilibrium concentrations of the matrix and dispersed phases, and f_e is the volume fraction at thermodynamic equilibrium. Equation (4), like Eq. (3), is valid in the limit of long aging times and predicts that f approaches f_e from below, i.e., f increases with aging time, equaling f_e when $t = \infty$.

Ideally, coarsening ceases at $t = \infty$, at which time all the solute is contained within a single particle. On its way to that eventuality, particles must disappear as the average size increases. The kinetics of this particle evanescence is described by the relationship

$$N_v \approx \frac{3f_e}{4\pi\psi kt}\left[1 - \frac{(\kappa t)^{-1/3}}{f_e\Delta X_e}\right], \tag{5}$$

where the parameter $\psi = \langle r^3\rangle/\langle r\rangle^3$ is determined by the PSD; for the LSW PSD, $\psi = 1.13$. Equation (5) follows from the relationship (for spherical particles)

$$\langle V\rangle N_v = \frac{4\pi\psi\langle r\rangle^3 N_v}{3} = f, \tag{6}$$

where $\langle V\rangle = 4\pi\langle r^3\rangle/3$ is the average volume of the particles. The parameter ψ must be considered because $\langle r^3\rangle \neq \langle r\rangle^3$. Substitution of Eq. (4) into Eq. (6) leads directly to Eq. (5). Equation (6) is unrelated to coarsening and is expected to be always valid. It has been common practice in the literature to ignore the second term in brackets in Eq. (5), but it has been shown repeatedly and convincingly that it is correct [3,4]. Equation (5) is expected to be valid in the very long time limit of an experiment, which often makes it quite difficult to test.

A singular prediction of the LSW theory is the equation for the scaled, time-invariant PSD given by

$$g(u) = \frac{4u^2}{9}\left(\frac{3}{3+u}\right)^{7/3}\left(\frac{3/2}{3/2-u}\right)^{11/3}\exp\left(\frac{-u}{3/2-u}\right); \quad u \leqslant 3/2. \tag{7}$$

In Eq. (7), u is the particle size scaled by the average size, i.e., $u = r/\langle r\rangle$, and $g(u)$ is a probability density function defined such that $g(u)du$ is the probability of finding a particle with scaled radius between u and $u + du$. It clearly follows that $\int_0^{3/2} g(u)\,du = 1$ and $\langle u\rangle = \int_0^{3/2} ug(u)\,du = 1$. The PSD described by Eq. (7) is skewed to the left, reaches a maximum value at $u \approx 1.13$, and has a very sharp cutoff at $u = \frac{3}{2}$.

Real systems differ from the ideal LSW system in many important ways: (1) the matrix phase is rarely an ideal infinitely dilute solid solution; (2) the dispersed phase is never a pure element but is instead a solid or liquid solution or compound; (3) the particles themselves are not always spherical; and (4) the volume fraction of the dispersed phase is always finite, which is important because the LSW theory is written for the physically unrealistic situation $f_e = 0$. In MDC coarsening, f_e plays an important role because the interparticle distances decrease as f_e increases, which implies that diffusive fluxes from shrinking to growing particles increase, ultimately leading to an increase in the rate constant for coarsening. The rate constant k is therefore expected to be a monotonically increasing function of f_e, i.e., $k = k(f_e)$. The finite volume fraction also engenders spatial correlations among the dispersed particles; these simply do not exist in the $f_e = 0$ limit of the LSW theory.

The effect of f_e on $k(f_e)$ in MDC coarsening has been the focus of numerous theoretical treatises. The interested reader is referred to several review articles that deal with this topic [5–8]. The subject continues to be of interest, as exemplified by several papers [9–11]. All the theories use as a model a spatially random dispersion of spherical particles which exchange atoms via diffusive transport in the matrix. It is fair to state that they all predict quite different dependencies of $k(f_e)$ on f_e but retain the temporal exponent $n = 3$ and agree with $k = k(0)$ in the limit of zero volume fraction.

It is also fair to state that most experimental investigations of particle coarsening in metallic alloys indicate no effect of f_e on coarsening behavior. To be sure, there are some exceptions; the coarsening of Co precipitates in aged Cu-Co alloys [12,13] and metastable $\delta'(Al_3Li)$ precipitates in Al-Li alloys [14] are the most obvious examples, but numerous experiments on the coarsening of γ' (Ni_3X) precipitates in Ni-X alloys (X = Al [13,15,16], Ga [17,18], Ge [19,20], Si [21–23], Ti [24,25]) show either no effect of f_e at all or an anomalous and still unexplained decrease of $k(f_e)$ with f_e at small volume fractions, typically $f_e < 0.08$ [20,21,24,26]. The most convincing evidence for the absence of an effect is embodied in the data on coarsening of Ni_3Si precipitates in Ni-Si alloys, wherein f_e varies by a factor of 10, from 0.03 to 0.30. The utter failure of theory to account for this behavior led Ardell and Ozolins [27] to seek a possible mechanism of coarsening consistent with the experimental results, culminating in the trans-interface-diffusion-controlled (TIDC) theory of coarsening.

A foundational premise of the TIDC coarsening theory is the diffuse nature of the particle-matrix interface. Atomistic simulations of the γ/γ' interface in Ni-Al alloys [28] showed that the interface between the face-centered cubic γ matrix and the ordered γ' precipitate was not sharp, but diffuse, transitioning over ~2 nm. In conjunction with the fact that diffusion in the ordered γ' phase is roughly two orders of

magnitude slower than in the disordered Ni-Al solid solution γ phase [29,30], this led to the expectation that diffusion through the interface should be much slower than diffusion to it, hence the taxonomy of TIDC coarsening. In the original publication by Ardell and Ozolins [27], the width of the interface δ was taken as constant, leading ultimately to a temporal exponent $n = 2$, with a hint of what we might obtain for temporal exponents satisfying $2 \leqslant n \leqslant 3$. This idea was elaborated more thoroughly in a subsequent paper [31] for arbitrary n and used to reexamine data on γ' coarsening in Ni-Al alloys, with $n \approx 2.4$ providing the best fit to the data on kinetics and the PSDs. This approach is employed in this paper to reexamine published data on coarsening of solid β-Sn particles in liquid Pb-Sn alloys. For the sake of completeness, when n is unknown, the temporal exponent three is replaced by n in Eqs. (1), (3), (4), and (5), with the factor kt in the denominator of Eq. (5) replaced by $(kt)^{3/n}$.

The interpretation of experiments on particle coarsening is often plagued by extraneous factors. Coherency strains are particularly important because they affect the equilibrium shapes of the particles as well as their spatial correlations. This is exemplified by the γ'-type precipitates in all the binary Ni-base alloys investigated [32]. Issues of this type simply vanish in solid-liquid (S-L) systems, since the host matrix is incapable of supporting shear strains and the particles will also be close to spherical in shape, provided that the S-L interfacial energy is nearly isotropic. This realization has provided the impetus for experiments on particle coarsening in S-L systems. Such experiments are not without their own set of drawbacks and complications, however.

A major obstacle to the successful implementation of terrestrial experiments on S-L coarsening is gravity, which induces either sedimentation or buoyancy, depending on the mass density difference between the solid and liquid phases. A dispersion of solid (or liquid) particles coarsening in a liquid matrix under conditions of microgravity can overcome this obstacle, provided that the S-L interfacial energy is isotropic. This realization stimulated several experiments on the coarsening of solid particles in liquid matrices. The earliest of this kind was done on solid Co particles in a liquid Cu matrix by Kang and Yoon [33] at temperatures from 1150 to 1300 °C. They chose the Cu-Co system because the two metals are nearly isopycnic, the mass density of Cu being slightly smaller than that of Co, 7900 cf. 8380 kg/m^3, at 1200 °C [34]. Kang and Yoon found that $k(f_e)$ was strongly dependent on f_e for volume fractions in the range $0.34 \leqslant f_e \leqslant 0.55$ at 1200 °C, increasing by a factor of 1.83. Bender and Ratke [34] investigated the coarsening behavior of solid Co particles in this system at 1200 °C over the range of volume fraction $0.25 \leqslant f_e \leqslant 0.70$ and found that $k(f_e)$ was nearly constant up to $f_e = 0.6$. The reasons for the discrepancy between their results and those of Kang and Yoon were not discussed by Bender and Ratke, who reported that sedimentation created a contiguous skeleton of Co particles very quickly for their range of volume fractions.

Seyhan *et al.* [35] performed experiments on the coarsening of Pb-rich particles in hypoeutectic Pb-Sn alloys. The idea behind these experiments was to suppress sedimentation by imposing Lorentz forces, engendered by electric and magnetic fields, on the liquid alloy system in a specially designed container that allowed for heating, isothermal aging, and relatively rapid cooling. The aged specimens were sectioned and polished for metallographic examination by scanning electron microscopy. Average particle sizes and distributions were then measured from the plane sections. The rate constants for coarsening were essentially constant for alloys containing 30, 40, and 50% Pb particles, but increased with f_e in alloys with volume fractions ranging from 0.57 to 0.71. Despite the incontrovertible constancy of $k(f_e)$ with increasing f_e from 0.3 to 0.5, the authors suggested that their data more or less confirmed an overall tendency of $k(f_e)$ to increase with f_e. We will comment on this issue later.

II. CRITICAL EVALUATION OF DATA ON COARSENING OF SOLID Sn PARTICLES IN LIQUID Pb-Sn ALLOYS

The most comprehensive investigations of L-S coarsening are those which constitute the focal point of the work described in this paper. They are the results of an extensive series of experiments performed under microgravity conditions which are described in several publications [36–39]. An avowed purpose of these experiments was to provide a true test of theory concerning the volume fraction dependency of $k(f_e)$ on f_e. Microgravity was deemed the antidote to sedimentation, buoyancy, and convection. Also, the low eutectic temperature in the Pb-Sn phase diagram ~183 °C [40] is advantageous because it is well established and low enough to mitigate the danger of experimental mishaps in a space shuttle or the International Space Station environment. Experiments were conducted at 185 °C for aging times ranging from 550 s to 48 h over a wide range of volume fractions in hypereutectic alloys, including 0.10, 0.15, 0.20, 0.30, 0.50, and a few larger values of f_e where solid Sn is the majority phase (the compositions of the alloys were not specified). The initial experiments were performed on two space shuttle missions. Subsequent experiments were performed on the International Space Station. The shortest aging time 550 s was limited by the time taken to reach the aging temperature, and the longest aging time was limited to 48 h due to temperature gradients in the furnace, but the duration varied from mission to mission. Many of the experimental details are presented in a report by Duval *et al.* [38]. Cooling from the annealing temperature was accomplished using a jet water spray, and the cooling curves indicated that the time to reach ambient temperature from 185 °C was ~35 s [38]. Nearly all the measurements of the particle sizes and PSDs were made on polished plane sections, but a few were done using a serial sectioning technique [39,41,42].

A. The kinetics of particle growth

The data on kinetics consisted primarily of measurements of average plane-section radii $\langle r_{ps} \rangle$ vs annealing time t and were presented in published figures. To extract the data as accurately as possible, the application WebPlotDigitizer was used to capture the data in a picture file, downloaded in .csv format. The data were then imported into Microsoft Excel and charted exactly as they were in the original picture file, which was also imported into the Excel worksheet. By superimposing a partially transparent picture file and the Excel chart, it is

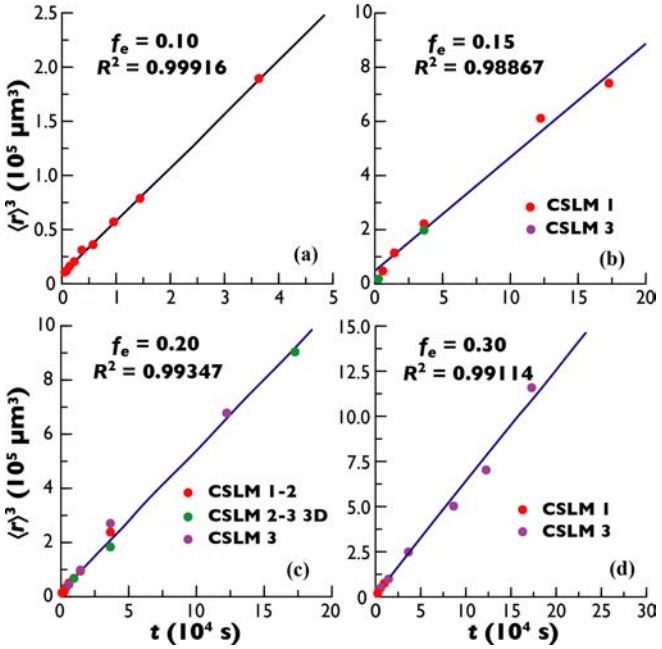

FIG. 1. The data of Thompson *et al.* [39] on the variation of the cube of the average particle radius $\langle r\rangle$ with aging time t. The missions, equilibrium volume fractions f_e, and correlation coefficients R^2 are shown in each figure.

possible to fine-tune the data to superimpose the two figures. We believe this procedure provides the most accurate possible representation of the published data, which were not available in tabulated form from the authors or from the National Aeronautics and Space Administration (NASA), which sponsored the research project.

Examination of the kinetics of particle growth was done by converting the two-dimensional (2D) data on $\langle r_{ps}\rangle$ to their three-dimensional (3D) counterparts. For spherical particles, it is necessary only to use the well-known result $\langle r\rangle = 4\langle r_{ps}\rangle/\pi$. However, Thompson *et al.* [39] found that the β-Sn particles in their alloys were not perfectly spherical and used a volume-fraction-dependent correction factor C_f to convert $\langle r_{ps}\rangle$ to $\langle r\rangle$, i.e., $\langle r\rangle = C_f\langle r_{ps}\rangle$. The reported values of C_f are 1.248 and 1.241 for $f_e = 0.15$ and 0.20, respectively. When $f_e = 0$, the reasoning of Thompson *et al.* suggests that $C_f = 4/\pi \approx 1.273$, and indeed a plot of C_f vs f_e is linear, resulting in the equation

$$C_f = -0.3628\, f_e + 1.2731. \tag{8}$$

In keeping with the spirit of the work of Thompson *et al.*, their data on $\langle r_{ps}\rangle$ in the alloys with $f_e = 0.10$ and 0.30 were also converted to $\langle r\rangle$ after substituting the appropriate value of f_e into Eq. (8).

Consideration of all results at face value yields the behavior on the kinetics of growth of the average particle shown in Fig. 1 for all volume fractions up to $f_e = 0.30$. The data are plotted assuming LSW kinetics, i.e., a linear dependence of $\langle r\rangle^3$ on t. The data are color-coded to distinguish the individual missions in the experiments, using the designations of the authors. The scales of the ordinates and abscissae were chosen to enable easy visual comparison of the slopes of the curves.

TABLE I. The rate constants $k(f_e)$ obtained from best fits to the data on each alloy in Fig. 1. The last row shows the value of $k(f_e)$ when the datum on 48 h in Fig. 1(d) is omitted.

f_e	$k(f_e)(\mu m^3/s)$
0.10	4.938 ± 0.064
0.15	4.195 ± 0.225
0.20	5.211 ± 0.134
0.30	6.268 ± 0.198
0.30	5.643 ± 0.078

The linear fits to the data exclude the measurements made at the smallest aging times, 550 and 880, since steady-state coarsening regime had not yet been obtained; their inclusion in the fitting has a negligible effect on the slopes of the curves. Even though the data on the longest aging time used in the experiments, 48 h, might have been compromised by temperature gradients in the furnace [36], they are included to eliminate any possible notion of bias in our analyses.

The rate constants $k(f_e)$ were obtained from the slopes of the curves in Fig. 1. They are tabulated in Table I and displayed as a function of f_e in Fig. 2. There is a very small increase in $k(f_e)$ with f_e, but we attribute this to the increasing role of coalescence as f_e increases. Lifshitz and Slyozov [1] recognized the potential role of coalescence, and Davies *et al.* [43] later constructed a theory of the effect of f_e on the kinetics of coarsening, assuming that, when two particles come into contact, they are instantly replaced by a single particle of the same volume as the original two. This is an impossible event for two solid particles. Indeed, there are numerous examples of particles in contact in the published micrographs of the solidified Pb-Sn microstructures [36,39,44–46]. It is nevertheless evident that coalescence will contribute to the augmentation of the kinetics of growth and almost

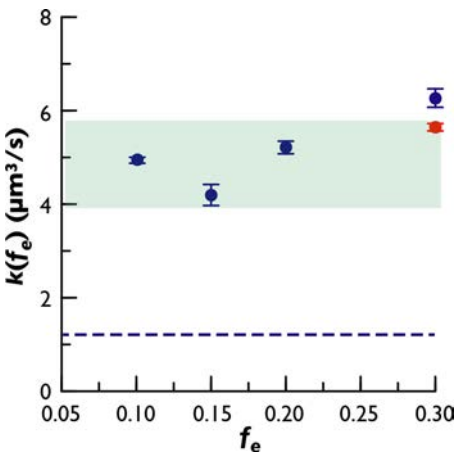

FIG. 2. The rate constants for coarsening $k(f_e)$ vs equilibrium volume fraction f_e for the four alloys. The dashed horizontal line represents the value of $k(0)$ measured independently from the grain-boundary grooving experiments of Hardy *et al.* [47]. The point represented by the filled red circle shows the value of $k(f_e)$ when the datum on 48 h, Fig. 1(d), is excluded. The shaded area in light green illustrates the small range of $k(f_e)$.

TABLE II. Number densities N_v and average radii $\langle r\rangle$ of Sn particles in the $f_e = 0.15$ and 0.20 alloys obtained from 2D (plane) and 3D sections. Aging time = 48 h.

Mission	f_e	$N_v(\mu\text{m}^{-3})$ (2D)	$N_v(\mu\text{m}^{-3})$ (3D)	$1/N_v(10^7\,\mu\text{m}^3)$ (2D)	$\frac{1}{N_v}(10^7\,\mu\text{m}^{-3})$ (3D)
CSLM-2R	0.15	3.75×10^{-8}	1.96×10^{-9}	2.67	51.02
CSLM-2R	0.20	3.41×10^{-8}	4.65×10^{-8}	2.93	2.15

certainly influence the PSDs. Having said this, it seems that only $k(f_e)$ for the alloy with $f_e = 0.30$ is somewhat larger than the values for the other three alloys. We note that the inclusion of the datum on the alloy aged for 48 h increases the calculated value of $k(f_e)$ by ∼10%; the difference between the slopes when the datum on 48 h is excluded is clear in Figs. 1(d) and 2 and Table I.

Hardy *et al.* [47] conducted grain-boundary grooving experiments on a eutectic Pb-Sn alloy for the expressed purpose of obtaining an independently measured value of $k(0)$ at 458 K, the reported value of which is 1.14 $\mu\text{m}^3/\text{s}$. It is evident in Fig. 2 that the experimentally measured values of $k(f_e)$ are significantly larger, by a factor of 4 to 5, than expected from the grain-boundary grooving experiments. This should not be surprising, since we assert that the $k(f_e)$ in Fig. 2 and Table I are simply the slopes of plots of $\langle r\rangle^3$ vs t and therefore have nothing to do with either LSW coarsening kinetics or grain-boundary grooving. We argue that the coarsening behavior of Sn particles is controlled by trans-interface diffusion, so in this sense the data on $k(f_e)$ are just numbers.

For the record, we note that the values of $k(f_e)$ reported in Table I are slightly larger than those reported by the authors of the numerous papers published under NASA support. The reason is that we take $k(f_e)$ from the slopes of plots of $\langle r\rangle^3$ vs t, which are completely unaffected by the magnitude of the constant of integration $\langle r_0\rangle^3$ in Eq. (1). This is not the case when $k(f_e)$ is determined by fitting data on the kinetics of growth to the equation $\langle r\rangle = [k(f_e)t - \langle r_0\rangle^3]^{1/3}$. Here, the output of whatever fitting routine is used inevitably includes (adversely we believe) the influence of the parameter $\langle r_0\rangle$, which has essentially no physical significance.

B. The kinetics of particle evanescence

There are two serious issues with the data on N_v vs t reported by Thompson *et al.* [39] that render reanalysis futile. The purpose of this small section is simply to make the reader aware that we are not sidestepping the reanalysis of their data. Most of the measurements were made on plane sections of the 15 and 20% alloys. These data are reported in plots of N_v^{-1} vs t. Thompson *et al.* also reported separate values of N_v and $\langle r\rangle$ for specimens of both alloys aged for 48 h, obtained from 3D serial sectioning. Those results are reported in the text along with detailed descriptions of the procedures used. A comparison of the values of N_v obtained using these two methods is presented in Table II. It is obvious that there are significant discrepancies between the 2D and 3D measurements. The reported value of $N_v = 1.96 \times 10^{-9}\,\mu\text{m}^{-3}$ is almost certainly an order of magnitude too small, since it is inconsistent with the reported details used in the 3D measurements. Even allowing for what is probably a misprint, the discrepancies are unacceptably large.

We cannot ascertain the cause of the large discrepancies presented in Table II, but it is also possible to check whether the data contained therein are consistent with the demands of Eq. (6). As stated earlier, Eq. (6) is quite general and must be obeyed, within experimental error, no matter what the mechanism of particle growth happens to be. To this end, the values of f were calculated using the reported values of N_v and $\langle r\rangle$, assuming spherical shapes and $\psi = 1.2$, the expectation being that the results should more or less accurately reflect the reported volume fractions $f_e = 0.15$ and 0.20. The results are presented in Fig. 3, where it is evident that some of the data cluster loosely around the expected values, but others deviate

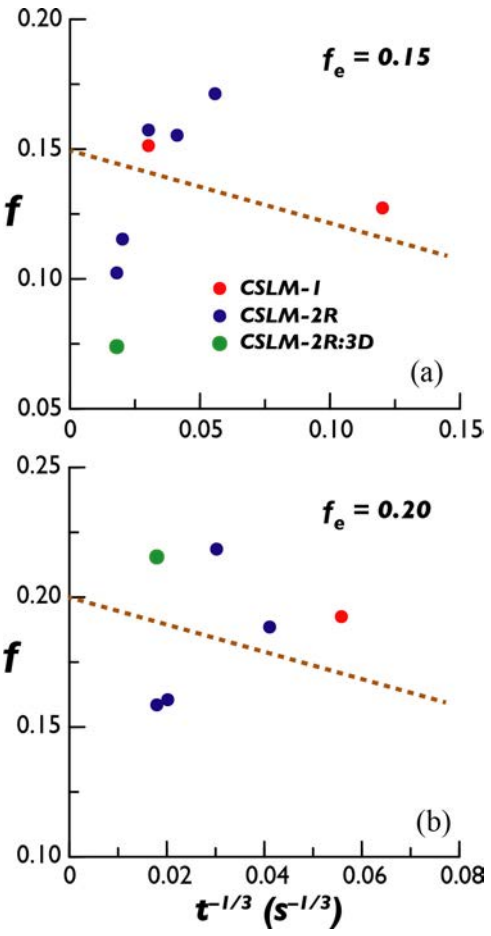

FIG. 3. Plots of the instantaneous volume fraction f vs aging time t raised to the $-\frac{1}{3}$ power for consistency with Eq. (4). The dashed lines in (a) and (b) are schematic, with intercepts representing f_e, but with arbitrary slopes. The data indicated by the filled green circles are the values of N_v reported in the text of Thompson *et al.* [39]. The color-coded data refer to the mission in which the experiments were done.

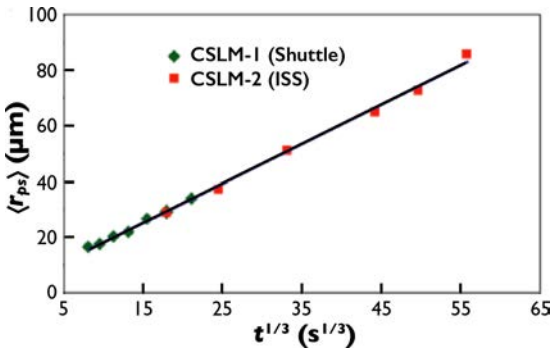

FIG. 4. Plot of the average planar particle radius $\langle r_{ps} \rangle$ vs aging time t raised to the $\frac{1}{3}$ power in the $f_e = 0.30$ alloy, reproduced from Duval *et al.* [35], but formatted for consistency with the other figures in this paper.

considerably. Much to our chagrin, we conclude, from the results reported in Table II and Fig. 3, that the discrepancies and uncertainties in the reported measurements of N_v are so large that no useful conclusions can be obtained from them.

C. Interpretation of the collective results of the coarsening experiments on Sn particles in liquid Pb-Sn alloys

One of the things that stands out most declaratively about the project on S-L coarsening in Pb-Sn alloy is the exquisite preparation of the experiments and the expertise with which they were conducted [36–38]. The methods used to characterize the microstructures and gather data were creative and innovative [41,42,46,48]. The examination of potentially spurious effects such as convection and g-jitter (residual accelerations under microgravity conditions) were deemed unimportant [49]. Moreover, the reproducibility of results from one mission to the next is remarkable, as attested to by the results in Fig. 4, reproduced directly from the report by Duval *et al.* [38], changing only the notation for consistency with this paper. These results were obtained from experiments on the $f = 0.30$ alloy over two different missions in which g-jitter was evaluated to have no influence on the data. The overlap between the average sizes from the two missions shows remarkable agreement. Only the datum on longest aging time, 48 h, shows any appreciable deviation from linear behavior in the plot of $\langle r_{ps} \rangle$ vs $t^{1/3}$. Indeed, even an inexperienced observer would conclude that these data are entirely consistent with steady-state LSW coarsening kinetics. To claim otherwise begs the question: how much additional aging time is needed to observe steady-state behavior? Nevertheless, in the final analysis, these data are not considered by Thompson *et al.* [39], dismissed [50] primarily due to the possible effects of particle contacts, which are to be expected in the alloy with $f_e = 0.30$ [43]. However, contacts among the Sn particles are present in the microstructures of all the Pb-Sn alloys investigated, as are deviations of the Sn particles from spherical shape and the influence of microgravity accelerations on sedimentation [49]. In fact, particle contacts and possible ensuing coalescence are most likely responsible for the increasing departure from sphericity with increasing f_e captured by Eq. (8). We see no compelling reason for dismissal of the data on the $f_e = 0.30$ alloy and include them in all the subsequent analyses.

Despite the excellent linearity of the data displayed in Fig. 1(a), the data on the $f_e = 0.10$ alloy were also dismissed from consideration by Thompson *et al.* [39]. The main reason given for rejecting those data was that coarsening occurred under conditions of transient coarsening kinetics [44,45,51]; it was also suggested that temperature gradients [52] might have played a role. However, the main reason for concluding that the data on the 10% alloy were occurring under transient coarsening conditions was the fact that the data failed to conform to the spatial correlations and PSDs predicted by the Akaiwa and Voorhees theory [53]. This is a highly unusual assertion because, when robust data do not fit a theory, the fault is generally not with the data but with the theory. The most logical conclusion is that there is either something wrong with the theory, or it simply does not apply to the specific conditions of the experiments. There is no question that the data on the kinetics of Sn-particle coarsening are robust and remarkably consistent from one mission to the next. We are inevitably drawn to the conclusion that all MDC coarsening theories fail to describe the data on coarsening of solid Sn particles in Pb-Sn alloys. We propose herein an alternative explanation, specifically that the data are consistent with the predictions of the TIDC theory of coarsening. We argue the case in the following sections but believe it is helpful to point out here that the mechanism of atom transport through a diffuse interface differs quite distinctly from mechanisms involving the rate-controlling attachment of atoms or molecules to atomically sharp interfaces, such as supported and/or colloidal nanoclusters [54–56].

III. THE CASE FOR TIDC COARSENING

A. Computer simulations of the solid Sn-liquid Pb-Sn alloy interface properties

The TIDC theory of coarsening [27] is predicated on the existence of a diffuse interface of width δ between the matrix and particle phases. Solute atoms must be transported through this interface to ensure growth or shrinkage of the particle itself. If diffusion in the particle phase is much slower than diffusion in the matrix phase, the kinetics of particle growth will inevitably be controlled by the slower process. Since the kinetics is controlled by diffusion through the interface rather than to it, there is no effect of volume fraction on the kinetics. The TIDC theory has been shown previously to account for the absence of an effect of volume fraction on the coarsening behavior of ordered γ' precipitates in Ni-base alloys, binary Ni-Al alloys [4,31] and ternary Ni-Al-Cr alloys [57] being representative examples. Moreover, in so-called "inverse" alloys, specifically binary Ni_3Al and Ni_3Ge alloys containing Ni-Al and Ni-Ge solid solution precipitates [58,59], the kinetics of coarsening is strongly dependent on f_e. In the inverse alloys, diffusion in the ordered matrix is much slower than in the interface. These findings are fully consistent with the demands of the TIDC theory.

Like the precipitate-matrix interfaces in γ/γ' alloys, S-L interfaces in alloys have also been shown to be diffuse, exemplified by numerous examples in a variety of different

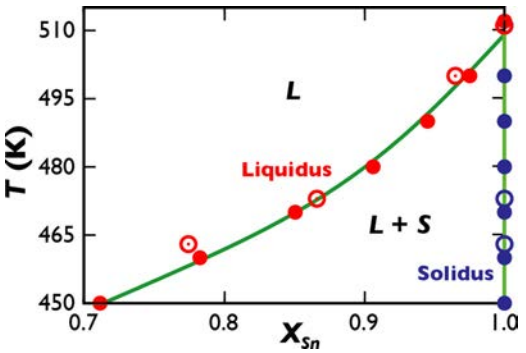

FIG. 5. The computed hypereutectic region of the Pb-Sn phase diagram (filled circles). The open circles represent points digitized from the phase diagram computed by Etesami *et al.* [71]. The letters L and L + S refer to the liquid and liquid + solid regions of the phase diagram.

alloys [60–70]. Although some computational modeling has been done on S-L Pb-Sn alloys [71], the widths of the solid-Sn/liquid Pb-Sn interface have not been previously modeled, thus providing the rationale for the research described in this section. We present here the main results, with many of the details described in Appendix A.

Atomic interactions in the Sn-Pb system were modeled using the modified embedded-atom interatomic potential developed by Etesami *et al.* [71]. Molecular dynamics (MD) and semigrand canonical Monte Carlo simulations (SGCMC) were performed with the Large-scale Atomic/Molecular Massively Parallel Simulator (LAMMPS[1]) [72]. To verify the methodology, we first reproduced the solidus and liquidus lines in the hypereutectic region of the Sn-Pb phase diagram, shown in Fig. 5, and found them to be in good agreement with the results of Etesami *et al.* [71]. As noted in Appendix A, there is no predicted solubility of Pb in solid Sn, which is due to the choice of the modified embedded-atom method (MEAM) potentials used in the simulations.

The interface properties were computed in a 16 000-atom simulation block containing the Sn-based solid phase and the liquid solution coexisting in thermodynamic equilibrium, separated by a planar S-L interface. Two interface orientations were modeled: (001) with the *c* axis of the tetragonal β-Sn structure normal to the interface and (010) with the *c* axis lying in the interface plane. The properties of the interface were characterized by profiles representing the Sn concentration, the energy density, and one of the bond order parameters across the interface plane. The atomic structures of the interfaces are shown in Fig. 6, and high-resolution profiles of the planar concentrations C_{Sn} across the interfaces at 458 K are shown in Fig. 7. Here, C_{Sn} is defined as the number of Sn atoms per unit volume in thin layers parallel to the interface plane (see Appendix A for details of the calculation of concentration profiles). The ragged nature of the interface is apparent in Fig. 6 and is consistent with variations in the planar concentrations seen in Fig. 7; these consist of sharp

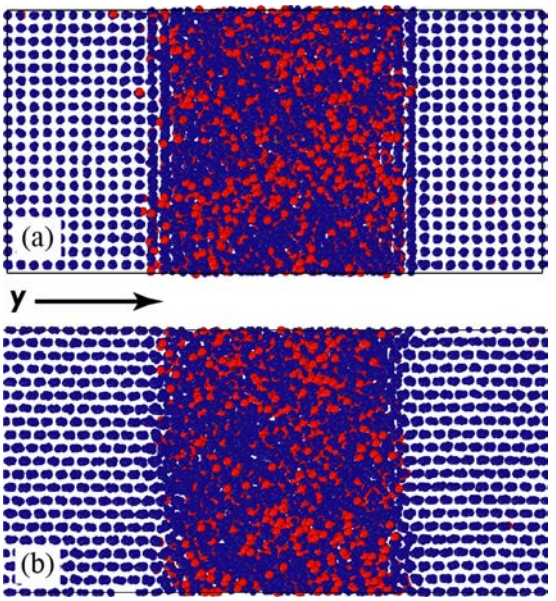

FIG. 6. Representative structures of the Sn-Pb solid-liquid coexistence system at 458 K for the (a) (010) and (b) (001) interfaces. The Sn and Pb atoms are shown in blue and red colors, respectively.

peaks corresponding to the crystal planes in the solid phase. It is evident that the transition from the solid phase (left) to the liquid phase (right) occurs over an interface region of ∼2 nm.

The Pb concentration profiles are shown in Fig. 8. The profiles were fitted to the results of the simulations using the

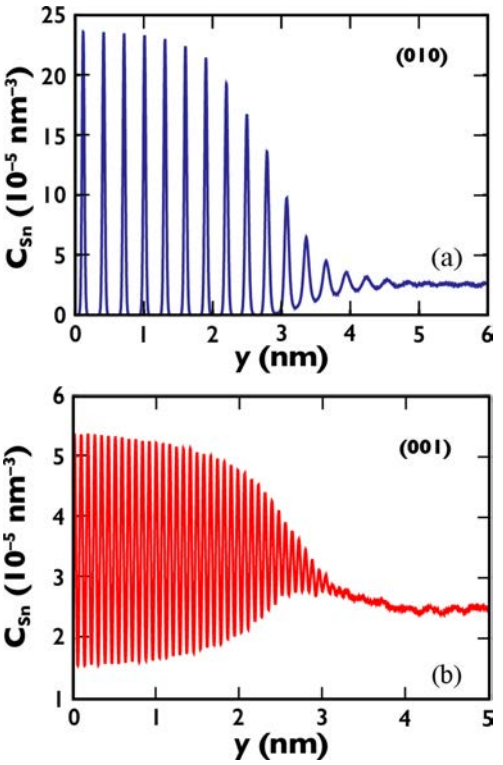

FIG. 7. Sn density profiles across the (a) (010) and (b) (001) interfaces for two interface orientations in the Sn-Pb system.

[1]The commercial names are used in this paper for completeness only and do not constitute an endorsement from NIST.

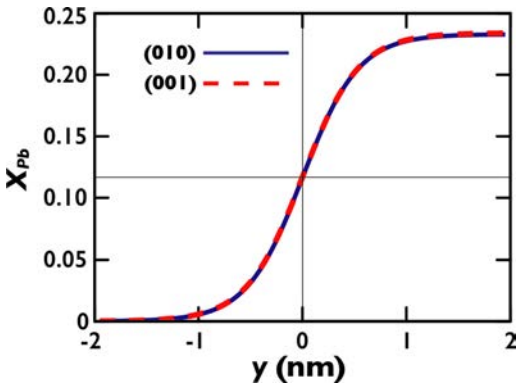

FIG. 8. The calculated Pb concentration $X_{\rm Pb}$ profiles across the solid-liquid interface for both orientations in the Sn-Pb system.

function

$$X_{\rm Pb} = \frac{X_{\rm Pb}^{\rm L} - X_{\rm Pb}^{\rm S}}{2}\left\{\tanh\left[\frac{2(y-y_0)}{w}\right]+1\right\} + X_{\rm Pb}^{\rm S}, \quad (9)$$

where $X_{\rm Pb} = X_{\rm Pb}(y)$ is the atom fraction of Pb as a function of distance y (see Fig. 6), $X_{\rm Pb}^{\rm L}$ is the equilibrium concentration of Pb in the liquid phase, $X_{\rm Pb}^{\rm S}$ is the equilibrium concentration of Pb in solid β-Sn, w is a parameter proportional to the interface width δ, and y_0 is the position of the interface. Equation (9) is a version of the more general Eq. (A1) in Appendix A, which is used to describe the variation of any property as a function of distance across the interface. To generate the curves in Fig. 8, the parameters substituted into Eq. (9) were $X_{\rm Pb}^{\rm L} = 0.233$, $X_{\rm Pb}^{\rm S} = 0$, and $y_0 = 0$, with $w \approx 1.08$ nm yielding the best fit to the simulated data (see Table III in Appendix A). On defining δ as the value of Δy corresponding to 1% differences between the equilibrium concentrations of Sn in the solid and liquid phases, we find $\delta \approx 1.7$ nm, or equivalently $\delta \approx 1.6w$. That the interface width is not sensitive to the orientation is consistent with the nearly spherical shape of the experimentally observed Sn particles, suggesting isotropic interfaces [39,50].

The simulations show that the S-L interfaces in the Sn-Pb system are not atomically sharp but rather extend over a width of ~1.7 nm. Interestingly, as shown in Appendix A, w decreases with increasing temperature, which is an unexpected finding that is not fully understood. It is perhaps not obvious in Fig. 8 at first glance, but the interface is not quite symmetric about $y = 0$, extending further into the liquid than in the solid. This might be an artifact of the absence of solubility of Pb in β-Sn in the simulations and is very likely an indication that the interface width is underestimated due to the chosen MEAM potentials.

TABLE III. Summary of the computed S-L coexistence properties of the Sn-Pb system at various temperatures. These include the liquidus and solidus compositions $X_{\rm Sn}^{\rm L}$ and $X_{\rm Sn}^{\rm S}$, the parameters w characterizing the (001) and (010) interfaces (indicated by the subscripts), and the equilibrium chemical potentials $\Delta\mu$ between Sn and Pb.

T (K)	$X_{\rm Sn}^{\rm L}$	$X_{\rm Sn}^{\rm S}$	$w_{(001)}$ (nm)	$w_{(010)}$ (nm)	$\Delta\mu$ (ev)
450.0	0.706	0.999	1.165	1.142	0.9541
458.0	0.766	0.999	1.087	1.077	0.9490
460.0	0.780	0.999	1.124	1.189	0.9471
470.0	0.850	0.999	1.149	1.039	0.9387
480.0	0.905	0.999	1.069	0.985	0.9275
490.0	0.948	0.999	0.913	0.916	0.9101
500.0	0.976	0.999	0.849	0.828	0.8816
511.5	1.000	1.000	–	–	–

B. Diffusion coefficients in the liquid and solid phases

In the case of coarsening of solid Sn particles in a liquid Pb-Sn matrix, the TIDC theory of coarsening predicts that the diffusion of Sn through the interface should be rate-controlling when $\langle r\rangle$ satisfies the condition (see Eq. (1) in [27])

$$\langle r\rangle \ll \delta\frac{\tilde{D}_L}{\tilde{D}_I}, \quad (10)$$

where $\tilde{D}_L$ is the chemical diffusion coefficient in the liquid, and $\tilde{D}_I$ is the average chemical diffusion coefficient in the interface region. Diffusion through the interface will certainly be dominated by diffusion in the solid phase, and we assert that, to a good approximation, $\tilde{D}_I$ can be replaced by $\tilde{D}_S$, the chemical diffusion coefficient in the solid.

To see this more clearly, consider the path of a Pb atom through the liquid into the solid region of the interface, the regions themselves acting as diffusion layers of infinitesimal thickness connected in series. For a composite structure consisting of individual layers of thickness δ_m, Crank [73] shows that the effective unidirectional diffusivity $D_{\rm eff}$ of the composite is obtained using the formula $\delta/D_{\rm eff} = \Sigma(\delta_m/D_m)$, where δ is the total thickness of the composite (which we identify here as the interface width), and D_m is the diffusion coefficient in each layer. Applying this reasoning to the problem of unidirectional diffusion through the S-L interface, we have $D_{\rm eff} = \langle\frac{1}{\tilde{D}_I}\rangle^{-1}$. Applying Eq. (A2), we obtain the result $\langle\frac{1}{\tilde{D}_I}\rangle = (\frac{1}{\tilde{D}_L} + \frac{1}{\tilde{D}_S})/2$. As we show in the following paragraph, $\tilde{D}_L \gg \tilde{D}_S$, hence, $D_{\rm eff} \approx 2\tilde{D}_S$. In this context, the factor of two is unimportant. For diffusion through layers in series, the layer with the smallest diffusion coefficient always dominates the effective diffusivity.

We have been unable to find any information at all on the diffusion of Pb in solid Sn, but since the solubility of Pb in solid Sn is quite small at the eutectic temperature ($X_{\rm Pb}^{\rm S} \approx 0.02$ [40]), the best we can do is use the data on self-diffusion of Sn at 458 K, 2 ° above the eutectic temperature. Chemical diffusion in the liquid containing $X_{\rm Pb} = 0.261$, the eutectic composition, is well represented by the data of Khairulin *et al.* [74] and Cahoon *et al.* [75], whose empirical representation of numerous sets of data support the conclusion of Khairulin *et al.* that diffusion in the liquid is essentially independent of composition. Self-diffusion in monocrystalline β-Sn has been measured by Meakin and Klokholm [76], Coston and Nachtrieb [77], and Huang and Huntington [78]. All these results, represented by calculations based on their empirical equations, are shown in Fig. 9. Also shown in Fig. 9 is the datum on the diffusivity cited by Hardy *et al.* [47], which was itself taken from the diffusion coefficients used by Jordan

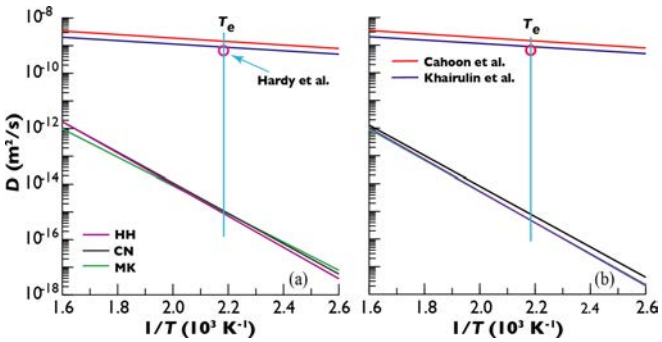

FIG. 9. Arrhenius plots of the data on the diffusion coefficients D in the liquid Pb-Sn phases and solid β-Sn. The curves on diffusion in the liquid were taken from the work of Khairulin *et al.* [74] and Cahoon *et al.* [75]. The curves on self-diffusion in solid β-Sn were taken from Meakin and Klokholm (MK [76]), Coston and Nachtrieb (CN [77]) and Huang and Huntington (HH [78]): (a) parallel to [001]; (b) parallel to [010]. The eutectic temperature $T_e = 456\,\mathrm{K}$ is indicated by the solid aqua line. The open circle shows the diffusion coefficient in the Pb-Sn liquid phase used by Hardy *et al.* [47] to evaluate the results of their grain-boundary grooving experiments.

and Hunt [79] to fit their data on the lamellar growth of the Pb-Sn eutectic.

Several facts are quite evident in Fig. 9: (1) the data on diffusion in the liquid phase are in quite good agreement; (2) the data on self-diffusion in β-Sn are also in good agreement for directions both parallel to, Fig. 9(a), and perpendicular to, Fig. 9(b), the c axis of the tetragonal β-Sn crystal structure; and (3) most importantly in the context of this paper, diffusion in liquid Pb-Sn alloys is 6 to 7 orders of magnitude faster than diffusion in solid Sn. Moreover, the diffusion of Pb in β-Sn should be much slower than Sn self-diffusion, given the significantly larger atomic size of Pb relative to Sn (175 pm cf. 140 pm). Applying Eq. (10) to the value of δ estimated from the atomistic modeling ($\sim$1.7 nm), we find that TIDC coarsening of β-Sn particles in a liquid Pb-Sn matrix of near eutectic composition should prevail for particle radii smaller than at least 1700 μm. This size is over an order of magnitude larger than the largest particle size reported by Thompson *et al.* [39]. This result, in conjunction with the absence of an effect of volume fraction on the kinetics of coarsening, completely justifies the reexamination of all data on coarsening of solid Sn particles in liquid Pb-Sn acquired under microgravity conditions. This reexamination follows.

C. The PSDs of the TIDC theory of coarsening—comparison with experimental data

1. *Evaluation of the PSDs and experimental cumulative distribution functions in S-L Pb-Sn alloys*

The PSDs play an important role in the TIDC theory of coarsening because fitting experimental histograms and experimental cumulative distribution functions (ECDFs) provide the most reliable way to evaluate the temporal exponent n, thereby paving the way for analyses of data on the kinetics of coarsening.

Thompson *et al.* [39] published PSDs for the $f = 0.15$ and 0.20 alloys aged for 48 h. A PSD for $f = 0.30$, also aged for 48 h, is reported in Thompson's Ph.D. dissertation [50] but was not included in Ref. [39]. Details of the evaluation of experimental histograms are presented in Appendix B. Foremost are the requirements that the area A under histogram constructed using the scaled variable u, as well as $\langle u\rangle$, must both equal unity. The criteria $A = 1$ and $\langle u\rangle = 1$ can be somewhat subjective if a visual fit to a theoretical PSD is all that is implemented for purposes of comparing experimental histograms with theoretical PSDs. More quantitative evaluation is necessary if a goodness of fit is attempted, as done herein. The extraction of both u and $g(u)$ from published histograms is fraught with uncertainties in the accuracy of plotting, small distortions introduced in printing, and the accuracy with which the data can be extracted from published figures. We point out here that small adjustments were needed to ensure that both A and $\langle u\rangle$ were equal to unity to within four significant figures, i.e., $A = \langle u\rangle = 1 \pm 0.0001$. For all three PSDs analyzed, the bin widths Δ were accurately reported, but small changes in $g(u)$ on the order of $\pm 1\%$ were required to ensure $A = 1$. On the other hand, the raw data extracted from the published histograms required more significant translations of the histograms to find the true zeros of the entire plot; we call these the zero offsets (ZOs). If the true origins of the histograms and theoretical PSDs do not coincide exactly, it is impossible to arrive at a valid quantitative analysis of the ECDFs. This issue is elaborated on further in Appendix B 2. For the Sn particle PSDs, the ZO was much smaller than the bin width.

The PSDs for the three alloys and aging conditions were converted to ECDFs for the purpose of applying the one-sample Kolmogorov-Smirnov (K-S) test [80]. The K-S test is widely used to test the null hypothesis in statistics where the data are drawn from a given theoretical distribution (e.g., a common default assumption is that the data follow the normal distribution) or, in the case of the so-called two-sample test, that there is no statistically significant difference between two datasets. In our case, the TIDC cumulative distribution function (CDF) $H(z)$ given by Eq. (B7) is used as the theoretical distribution; expressed in terms of the variable u, the theoretical CDF, $G(u)$ is known to be equivalent to $H(z)$ [81]. The K-S test statistic is calculated as the largest absolute deviation D_N, otherwise known as the supremum $\sup_u$ between the ECDF, $G_N(u)$, and $G(u)$,

$$D_N = \sup_u |G_N(u) - G(u)|. \tag{11}$$

When statistical data involve measurements of a discrete statistical property (millimeters of rainfall in a community, positive outcomes of a medical testing protocol, for example), $G_N(u)$ is calculated using the equation

$$G_N(u) = \frac{1}{N}\sum_{i=1}^{N} \theta(u - u_i), \tag{12}$$

where N is the number of measured entities, u_i represents the scaled magnitudes of the entities, and θ is the Heaviside function. The value of the K-S test statistic is that it is used to derive the p value of a test distribution; the p value is a parameter that quantifies the probability that the data could have been produced by a random sampling from the assumed theoretical CDF. A typical p value of 5% is used as the

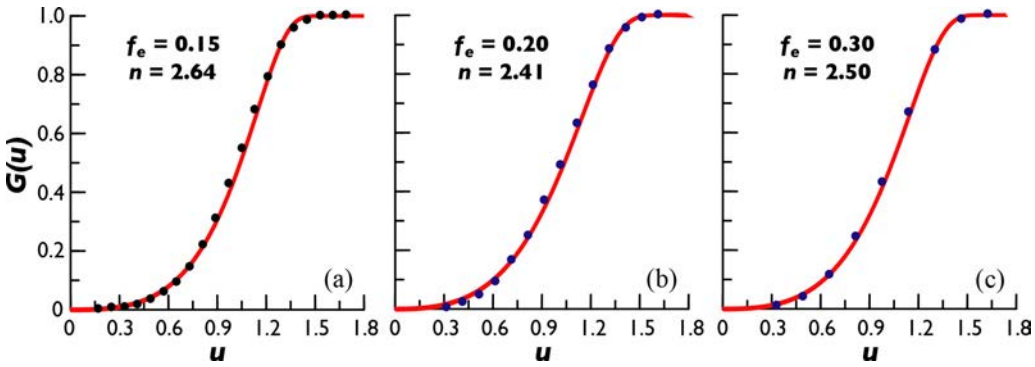

FIG. 10. Plots of the experimental cumulative distribution functions (ECDFs) and the theoretical cumulative distribution functions (CDFs) of the trans-interface-diffusion-controlled (TIDC) theory (red curves) $G(u)$ vs $u = r/\langle r\rangle$ for the three distributions reported by Thompson *et al.* [39] and Thompson [50]. The zero offsets in (a), (b), and (c) were −0.052, −0.065, and 0.088, respectively. The values of n resulting from the Kolmogorov-Smirnov (K-S) tests, shown in each figure, were used to compute $G(u)$ and are identical to the values of $n_{\rm opt}$ shown in Table IV.

threshold below which the null hypothesis is rejected and a conclusion is made that the data are unlikely to be drawn from the theoretical distribution.

When the entities in question are the sizes of individual particles, we can use Eq. (12), in conjunction with $G(u)$ of the TIDC theory, itself calculated for different trial values of the temporal exponent n, to calculate D_N. Unfortunately, published data on particle size statistics do not include all the measurements made on individual particles. There are many reasons for this, some having to do with the measurement procedures themselves and others having to do with the limitations of older publications where it was awkward or unacceptable to present many pages of tabulated data. Instead, typical statistical data are presented in the form of histograms, and our only recourse is to make use of them. Unfortunately, Eq. (12) cannot be applied to statistical data in the form of histograms, so to implement the K-S test, it is necessary to devise an alternative procedure. As explained in Appendix B 3, we use Monte Carlo simulations to generate a statistical population of particles based on the theoretical PSD of the TIDC theory, with specific values of n as the input parameter. We then calculate the K-S test statistic using the ECDFs constructed using Eq. (B12).

The results are shown in Figs. 10 and 11. The optimum values of n were obtained from the K-S fit (see Appendix B 3) and then used to calculate the theoretical PSDs. It is evident in Fig. 10 that the visual fits between $G(u)$ and the ECDFs are superb. The fits between $g(u)$ and the experimental histograms, Fig. 11, are also excellent. They are certainly at least as good if not better than the variety of theoretical PSDs chosen by Thompson *et al.* [39] to compare with their PSDs. In addition to a stronger basis in the theory of probability, it is clearly seen in Figs. 10 and 11 that, from a purely quantitative perspective, the fitting of ECDFs is far superior to fitting the PSDs.

TABLE IV. Fitted values of the parameters $n_{\rm opt}$, $D_N^{\rm ECDF}$, and p values for the three ECDFs generated from the histograms of Thompson *et al.* [39] using K-S test statistics in conjunction with the Monte Carlo simulations.

f_e	N	$n_{\rm opt}$	$D_N^{\rm ECDF}$	p value
0.15	773	2.64 ± 0.07	3.1%	12.5%
0.20	1380	2.41 ± 0.05	2.3%	11.2%
0.30	1887	2.50 ± 0.04	1.6%	18.7%

2. *The kinetics of particle growth*

In the TIDC theory, the equation for the kinetics of growth of a particle of average radius is given by Eq. (1), but with the temporal exponent three replaced by an unknown exponent n, which satisfies the condition $2 \leqslant n \leqslant 3$. In this case, Eq. (1) becomes

$$\langle r\rangle^n - \langle r_0\rangle^n = k_n t, \tag{13}$$

where the rate constant k_n also depends on n and the thermodynamic and kinetic parameters of the system, but does not depend on f_e. Here, k_n depends on the ratio $\tilde{D}_I/\delta$, both of which can vary with r. The assumption $\delta \propto r^m$ leads directly to Eq. (13), with $0 \leqslant m \leqslant 1$ and $n = m + 2$ [31]. This relationship demands that δ increases slowly as the particle radius increases, reaching the flat-interface value at $t = \infty$, i.e., the simulated value for the flat interface $\delta = 1.7$ nm. On the other hand, the concentration dependence of solute diffusion near the interface can also produce a result that depends on r^m [82]; this also leads to Eq. (13), but with k_n differing for the two different physical processes. We do not have enough information on the size dependence of δ or diffusive transport through the interface to know their relative importance but are confident that, in concert, they justify the existence of a temporal exponent that differs from three.

The kinetics of solute depletion, volume-fraction augmentation, and particle evanescence also depend on n, but as we have demonstrated, the kinetics of particle evanescence reported by Thompson *et al.* [39] were not reported accurately, so we must rely on analyses of the PSDs and kinetics of particle growth to examine how well the TIDC theory of coarsening describes the data. Using as a compromise the average value $n = 2.5$ originating from fitting the ECDFs, Fig. 10, the data of Thompson *et al.* [39] are shown in Fig. 12, where they are plotted as $\langle r\rangle^n$ vs t, for consistency with Eq. (13). The axes in Fig. 12 are scaled so that the slopes can

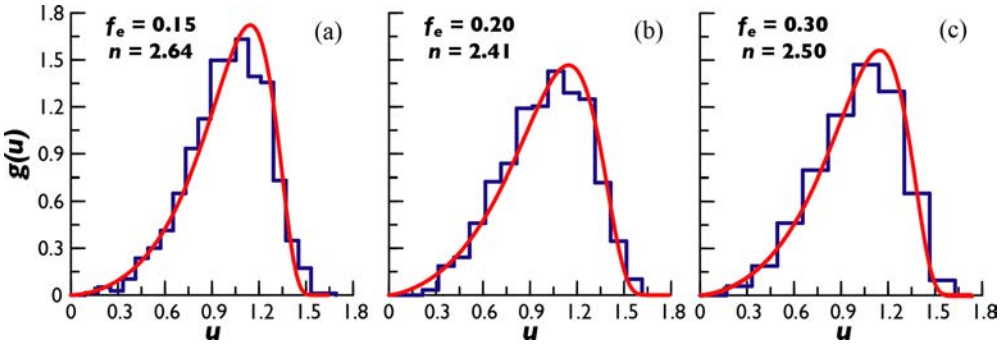

FIG. 11. The theoretical particle size distributions (PSDs), $g(u)$, of the trans-interface-diffusion-controlled (TIDC) theory (red curves) superimposed on the histograms for the three alloys. The three figures correspond to those in Fig. 10, with the same zero offsets.

easily be compared visually. As is the case for MDC coarsening $n = 3$, the slopes are roughly equal, k_n being the smallest for the $f_e = 0.15$ alloy and largest for the $f_e = 0.30$ alloy. Except for the $f_e = 0.30$ alloy, the correlation coefficients are slightly smaller than those in Fig. 1.

3. *Implications for data on coarsening in other S-L alloy systems*

The data on the coarsening of solid Pb alloy particles [35] in liquid Pb-Sn alloys and solid Co particles in liquid Cu-Co alloys [33,83] are the only other datasets that can be considered moderately extensive. The data of Seyhan *et al.* [35] are, at best, in only semiquantitative agreement with the predictions of the "first-principles" theory of Akaiwa and Voorhees [53] and the "effective-medium" theories of Marsh and Glicksman [84] and Brailsford and Wynblatt [85]. Seyhan *et al.* [33] considered numerous reasons why quantitative agreement was elusive, offering the following thought late in the Discussion Section of their paper, to wit: "Finally, of course, the reason for the disagreement between theory and experiment could be that the theory is inadequate." Of all

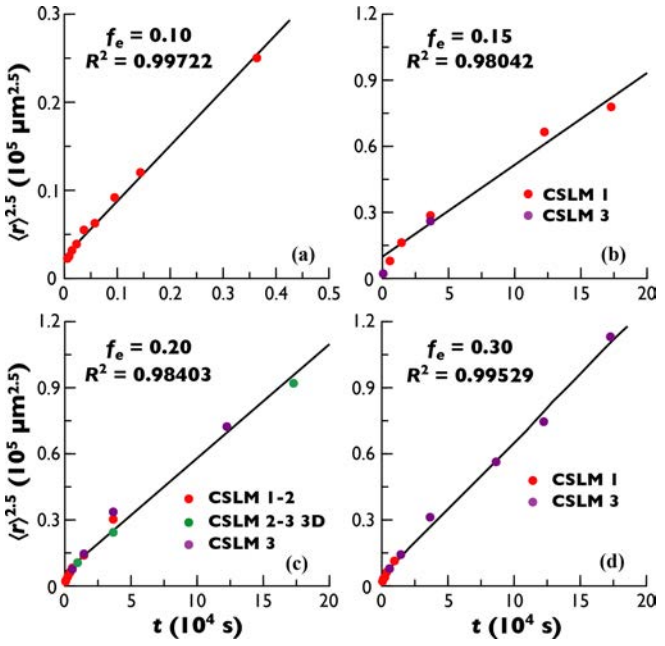

FIG. 12. The data of Thompson *et al.* [39] showing the dependence of the average particle radius $\langle r \rangle$ raised to the $n = 2.5$ power with aging time t. The missions, equilibrium volume fractions f_e, and correlation coefficients R^2 are shown in each figure.

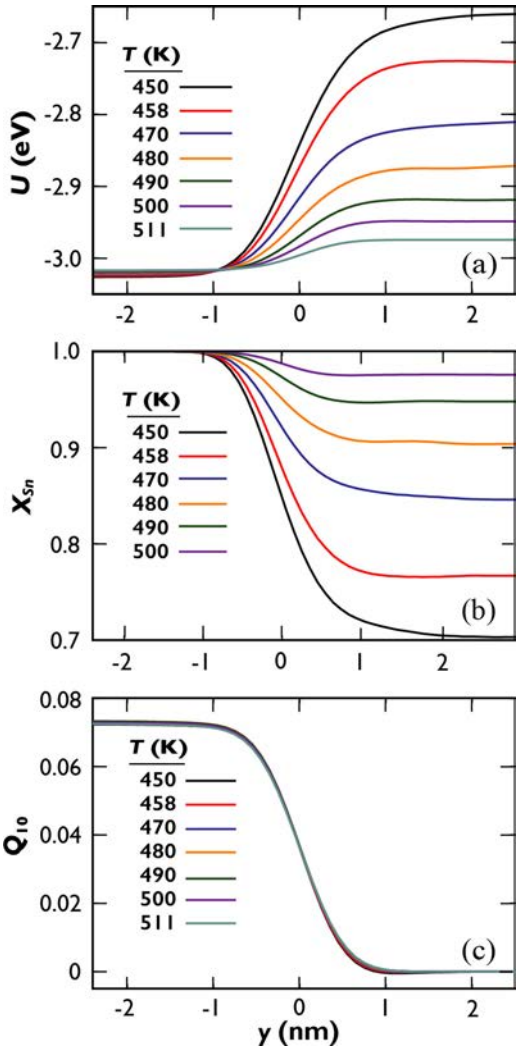

FIG. 13. The profiles of (a) energy, (b) atom fraction of Sn, X_{Sn}, and (c) order parameter Q_{10} across the (001) solid-liquid interface in the Sn-Pb system.

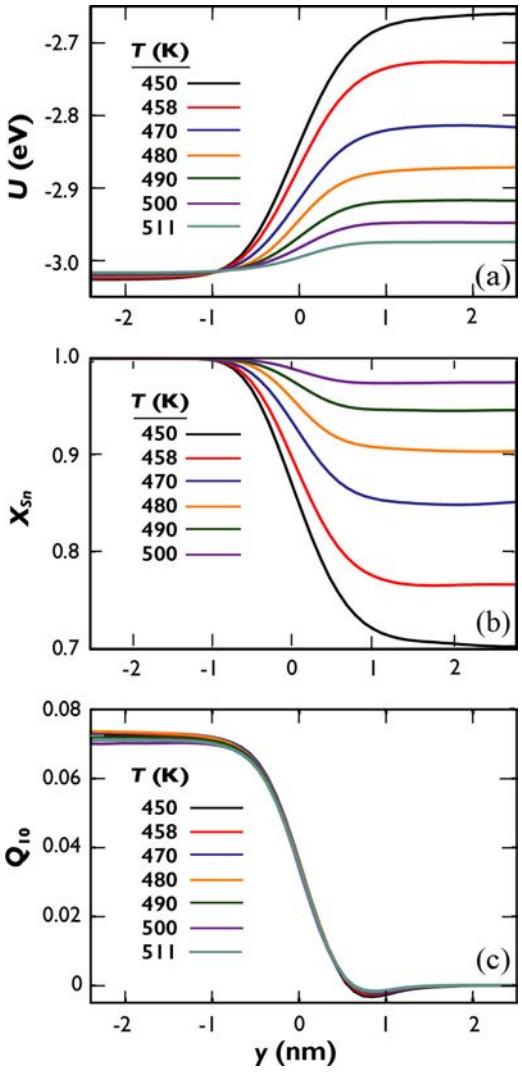

FIG. 14. The profiles of (a) energy, (b) atom fraction of Sn, X_{Sn}, and (c) order parameter Q_{10} across the (010) solid-liquid interface in the Sn-Pb system.

the possible suggestions, we find this one to be the most plausible. The TIDC theory of coarsening did not yet exist at the time of publication of the paper by Seyhan *et al.* [33], so they bear no blame or fault in not considering it. We suggest that the constancy of their measured rate constants for growth of the average particle, for their alloys containing 30, 40, and even 50% solid Pb alloy particles, is fully consistent with the predictions of the TIDC coarsening theory. Additional work remains to be done to confirm this conjecture, for example, atomistic investigations of the Pb(Sn)-liquid interface, measurements of the PSDs in 3D, and potentially useful experiments on the kinetics of solute depletion in aged specimens.

The conflicting results of experiments on the coarsening of solid Co particles in S-L Cu-Co alloys [33,83] cannot be untangled from the results of this investigation. As is the case for the solid Pb-liquid alloy system, far more work remains to be done, mirroring the work mentioned in the previous paragraph.

IV. SUMMARY

(1) We have demonstrated that the data on the kinetics of particle growth, taken at face value and analyzed according to the LSW theory, Eq. (1), indicate that the rate constants for coarsening are essentially independent of the volume fraction of solid β-Sn particles. This is especially true for the data on the $f_e = 0.10$, 0.15, and 0.20 alloys. It is also most probably true for the $f_e = 0.30$ alloy, where the rate constant $k(f_e)$ is slightly larger than for the other three (see Table I), due most likely to the increased role of coalescence in the higher volume fraction alloy and the influence of the single datum on 48 h of aging, see Figs. 1(d) and 4.

(2) Apart from the fact that the slopes of plots of $\langle r\rangle^3$ vs t are essentially independent of f_e, advocacy of the TIDC theory of coarsening is supported by several other findings. Atomistic simulations of the interface between the liquid of eutectic composition and solid β-Sn particles show that the width of the interface is $\sim$1.7 nm at 458 K. Using the best data available on diffusion of Pb in the solid and liquid phases in the eutectic system, we show that this value of δ is fully consistent with the condition $\langle r\rangle \ll \delta\tilde{D}_L/\tilde{D}_I$, Eq. (10), that formalizes the maximum particle size below which TIDC coarsening is valid. Specifically, $\langle r\rangle$ should be $<\sim$1700 μm, an average particle radius which far exceeds the largest average radius reported in the Pb-Sn coarsening experiments ($\sim$100 μm).

(3) The PSDs and especially the ECDFs are in excellent agreement with those predicted by the TIDC theory. In fact, our calculations show that the ECDFs pass the one-sample K-S test, which indicates that the experimental histograms are well described by the theoretical TIDC PSDs. To the best of our knowledge, this finding is unique for experimental statistical data on coarsening in alloys and furthermore emphasizes the importance of analyzing the ECDF quantitatively rather than relying on visual comparison between experimental histograms and theoretical PSDs.

V. CONCLUSIONS

Based on all the analyses of the data on coarsening of solid β-Sn particles in liquid Pb-Sn alloys obtained under conditions of microgravity, there is only one possible conclusion, and it is inescapable; the data are completely consistent with the TIDC theory of coarsening.

ACKNOWLEDGMENTS

J.F.H. and Y.M. acknowledge support from the Materials Science and Engineering Division, National Institute of Standards and Technology. V.O. acknowledges financial support from the National Science Foundation Grant No. DMR-1611507. A.J.A. thanks Professor Peter W. Voorhees, Northwestern University, for clarification of the discrepancy between the values of N_v reported in the text of Thompson *et al.* [39] and those in fig. 3 of their paper.

APPENDIX A: SIMULATION OF S-L INTERFACES IN THE Sn-Pb ALLOY SYSTEM

1. Simulation geometry and atomic interactions

The β-Sn structure was constructed using the conventional unit cell with the lattice vectors $\mathbf{A}_1 = a\mathbf{x}$, $\mathbf{A}_2 = a\mathbf{y}$, and $\mathbf{A}_3 = c\mathbf{z}$, where a and c are the lattice constants of the tetragonal unit cell and $\mathbf{x}$, $\mathbf{y}$, and $\mathbf{z}$ are unit vectors. The basis vectors have the lattice coordinates $\boldsymbol{b}_1 = (0, 0, 0)$, $\boldsymbol{b}_2 = (\frac{1}{2}, \frac{1}{2}, \frac{1}{2})$, $\boldsymbol{b}_3 = (0, \frac{1}{2}, \frac{1}{4})$, and $\boldsymbol{b}_4 = (\frac{1}{2}, 0, \frac{3}{4})$; for example, $\boldsymbol{b}_2 = \frac{1}{2}\mathbf{A}_1 + \frac{1}{2}\mathbf{A}_2 + \frac{1}{2}\mathbf{A}_3$. The S-L coexistence simulations used a simulation block containing the solid and liquid phases separated by a plane interface. Two cases were considered, with the interface plane being parallel to either the (001) or (010) crystallographic planes of the solid phase. In both cases, the interface normals were aligned with the y axis of the Cartesian coordinate system (see Fig. 6). The simulation block had the dimensions of 5.914 × 12.947 × 5.914 nm for y normal to (001) and 5.914 × 11.828 × 6.473 nm for y normal to (010). The number of atoms was 16 000 in both simulations.

Atomic interactions in the Sn-Pb system were described by the MEAM potential developed by Etesami *et al.* [71]. For simulations involving only Sn atoms, we used MD in the appropriate statistical ensembles as detailed below. The MD integration step was 1 fs. For the binary Sn-Pb system, the SGCMC method was used. The latter was implemented in the hybrid MC/MD mode [72] with 250 swap attempts after every 250 MD steps. Other combinations of the swap attempts and MD steps were also tested, and the results were found to be insensitive to these choices. The atomic structures and chemical distributions were visualized using the Open Visualization Tool (OVITO) [86].

As a test of methodology, the energy of the β-Sn structure was minimized with respect to atomic positions and the unit cell dimensions. The minimum energy was found to be −3.0901 eV with $a = 0.5914$ nm and $c = 0.3236$ nm, giving $c/a = 0.5473$. These values are in excellent agreement with the results of Etesami *et al.* [71].

2. Phase diagram calculations

The first step of the work was to verify our methodology by computing the solidus and liquidus lines on the Sn-rich side of the Sn-Pn phase diagram using the phase coexistence method [28,87–92]. The simulations were performed on the S-L systems with the (001) interface orientation, but this choice cannot possibly affect the results since thermodynamic equilibrium between bulk phases does not depend on the interface crystallography.

The system was brought to thermodynamic equilibrium by hybrid SGCMC simulations in the NPT ensemble (fixed number of atoms, temperature, and zero pressure). At a chosen temperature, a series of simulations was performed at different values of the chemical potential difference $\Delta\mu$ between Sn and Pb. At each $\Delta\mu$, the system energy was recorded as a function of time. The energy increased or decreased with time, depending on whether the solid phase was growing or melting. The rate of the energy change as a function of $\Delta\mu$ was calculated and interpolated to zero to find $\Delta\mu$ corresponding to the two-phase equilibrium. Typical structures of the equilibrium S-L systems are illustrated in Fig. 6. The chemical compositions of the coexisting solid and liquid phases $X^{\mathrm{S}}_{\mathrm{Sn}}$ and $X^{\mathrm{L}}_{\mathrm{Sn}}$ were obtained by separate single-phase NPT SGCMC simulations on smaller systems with the equilibrium value of $\Delta\mu$. The simulations were repeated at several temperatures to obtain the functions $X^{\mathrm{S}}_{\mathrm{Sn}}(T)$ and $X^{\mathrm{L}}_{\mathrm{Sn}}(T)$ describing the solidus and liquidus lines on the phase diagram. The diagram obtained is shown in Fig. 5 and agrees well with the hypereutectic liquid + solid region of the Pb-Sn phase diagram calculated by Etesami *et al.* [71]. Any minor discrepancies are likely to be due to the difference in the size of the simulation block. Note that the MEAM [71] potential underestimates the solubility of Pb atoms in the solid Sn phase in comparison with the experimental phase diagram [40].

Finding the melting temperature T_m of single-component Sn required a separate calculation since the SGCMC method was not applicable. In this case, NPT MD simulations were performed on the same S-L system as above but with Sn atoms only. Again, the rate of energy change was recorded for a set of different temperatures and interpolated to zero to obtain T_m. The melting temperature of Sn predicted by this potential $T_m = 511$ K is close to the value $T_m = 510$ K reported by Etesami *et al.* [40] but exceeding the experimentally measured melting temperature of ∼505 K.

3. Analysis of the S-L interface properties

The S-L interfaces are characterized by various properties, described by the generic variable $P(y)$, which varies throughout the interface region from the liquid to the bulk solid. The interface properties are presented as profiles of $P(y)$ vs y, where $P(y)$ is calculated by averaging the property over thin layers parallel to the interface. Two choices of the layer width were utilized. For the atomic density profiles, $P(y) = C_{\mathrm{Sn}}(y)$, where resolution of individual crystallographic planes was required, the layer width λ was chosen to be 0.001 nm. We define C_{Sn} using the formula $C_{\mathrm{Sn}} = N_{\mathrm{Sn}}/\lambda A_s$, where N_{Sn} is the number of Sn atoms in the layer, and A_s is the cross-sectional area of the simulation block. Within each layer, C_{Sn} was averaged in time throughout a 1 ns long simulation run. Since the interface location did not change on this timescale, the density profiles did not require recentering. The results of these simulations are shown in Fig. 7. The Pb layer concentration C_{Pb} was also obtained as part of the same calculation.

For other properties, smoother profiles were computed by choosing a larger layer size of 0.2 nm. Such properties included the potential energy U of the atomic interactions, the chemical compositions, and the bond-order parameters Q_i of Steinhardt *et al.* [93] for $i = 4$, 6, 8, 10, and 12 implemented in LAMMPS. The profile $P(y)$ of each property was averaged over 20 000 instantaneous profiles computed from snapshots saved during a 10 ns long MD run. To eliminate the effect of any possible drift of the average interface position, the instantaneous profiles were recentered to the same position before averaging. To this end, each instantaneous profile was fitted using the analytic function

$$P(y) = \frac{P_{\mathrm{L}} - P_{\mathrm{S}}}{2}\left\{\tanh\left[\frac{2(y - y_0)}{w}\right] + 1\right\} + P_{\mathrm{S}}, \qquad \text{(A1)}$$

where P_L and P_S are the values of the property in the liquid and solid phases, respectively, and w is related to the width of the interface. As in the previous work [91], the profiles were smoothed before fitting by averaging the data points with their nearest neighbors to reduce the thermal noise. Next, all the profiles were superimposed by shifting them to the same interface position y_0 (recentering), and the final profile was obtained by computing the moving average over this superposition. The Q_i profiles were additionally shifted by the same amount to achieve a zero value of the respective order parameter in the liquid phase. This shift did not affect the interface width and only served to clarify the presentation.

The average value of any property through the interface region $\langle P\rangle$ is readily calculated using the formula $\langle P\rangle = \delta^{-1}\int_{-\delta/2}^{\delta/2} P(y)dy$. On performing the integration using Eq. (A1) with $y_0 = 0$, we obtain the general result

$$\langle P\rangle = \frac{P_L + P_S}{2}. \tag{A2}$$

Applying Eq. (A2) to obtain the average concentration of Sn in the interface region, for example, we find $\langle X_{Sn}\rangle = (X_{Sn}^L + X_{Sn}^S)/2$, which is an illustrative though unsurprising result.

For the chemical composition profiles, $P_L = X_{Sn}^L$ and $P_S = X_{Sn}^S$, the magnitudes of which were determined from the calculations of the phase diagram. We preferred to present the composition profiles in Fig. 8 using $X_{Pb}(y)$ rather than $X_{Sn}(y)$ since the traditional representation of composition profiles in coarsening processes involves the minority component. Equation (9) follows from Eq. (A1) on using the relationship $X_{Pb}(y) = 1–X_{Sn}(y)$. Table III summarizes the S-L coexistence properties computed as a function of temperature. The equilibrium chemical potential difference $\Delta\mu$ is included for reproducibility of the results. The first three columns of the table allow the reader to reconstruct the relevant part of the computed phase diagram, Fig. 5. The last line reports the Sn melting temperature.

In order to model the hypereutectic region of the Pb-Sn phase diagram it was essential to compute the profiles of the local energy per atom, U, the concentration of Sn, X_{Sn}, and the bond order parameter Q_{10} across the L-S interface as functions of temperature. The results of these computations are shown as the profiles across the (001) and (010) interfaces over the temperature range 450 to 511 K in Figs. 13 and 14.

APPENDIX B: PSDS AND CUMULATIVE DISTRIBUTION FUNCTIONS

1. Theoretical considerations

The probability density function predicted by the LSW theory is represented by Eq. (7). Generalization to the TIDC theory requires some background information. In a polydisperse array, large particles grow at the expense of small ones, and there exists a critical radius r^* which is momentarily neither growing nor shrinking at time t; r^* depends on t in the same way that $\langle r\rangle$ does, but r^* and $\langle r\rangle$ are not necessarily equal. In all theories of coarsening, the initial scaling of the PSD is expressed in terms of the variable $z = r/r^*$, the probability that the radius of a particle lying between r and $r + dr$ equaling the probability that the scaled radius lies between z and $z + dz$; this probability is $h(z)dz$. Since r^* is not generally measurable, experimental data on PSDs are expressed in terms of the scaling variable $u = r/\langle r\rangle$. Comparison between experimentally measured and theoretical PSDs therefore requires knowledge of the relationship between r^* and $\langle r\rangle$. It follows from the definitions of u and z that $u = z/\langle z\rangle$, where $\langle z\rangle = \langle r\rangle/r^*$ is the first moment of the theoretical probability density function $h(z)$, which generally differs from $g(u)$. In most situations, we need to convert $h(z)$ to $g(u)$ to compare experimental histograms with theory. Given that $h(z)dz = g(u)du$, it follows that $g(u) = h(z)dz/du = \langle z\rangle h(z)$. In the special case of MDC coarsening, it happens that $r^* = \langle r\rangle$ [1,2], so that $z = u$, $g(u) = h(z)$, and $\langle z\rangle = \langle u\rangle = 1$.

An important feature of the TIDC theory is that n related to the theoretically predicted PSD $h(z)$ through the equations [25]

$$h(z) = -3\phi(z)\exp\{\xi(z)\}, \tag{B1}$$

$$\xi(z) = 3\int_0^z \phi(x)dx, \tag{B2}$$

and

$$\phi(z) = \frac{z^{(n-1)}}{(z-1)[n^n/(n-1)^{(n-1)}] - z^n}, \tag{B3}$$

where the factor of three in Eq. (B2) was inadvertently omitted. In statistical terms $h(z)$ is a one-parameter probability density function in the sense that all second and higher moments are determined uniquely by the value of n.

Analytical solutions to the system of Eqs. (B1)–(B3) are possible only for $n = 2$ (IRC coarsening) and $n = 3$ (the LSW case). The PSD for IRC coarsening $n = 2$ was published by Wagner [2]; the equation is

$$h(z) = \frac{24z}{(2-z)^5}\exp\left(\frac{-3z}{2-z}\right); \quad z \leqslant 2. \tag{B4}$$

Interestingly, Eq. (B4) is identical to the PSD derived by Hillert [94] for the process of 3D grain growth, the kinetics of which is also governed by Eq. (2). To illustrate the difference between $g(u)$ and $h(z)$, we first note that $\langle z\rangle$ for IRC coarsening is $\frac{8}{9}$ [2], hence, $u = \frac{9z}{8}$. Equation (B4) expressed in terms of the scaling variable u is therefore

$$g(u) = \frac{(3/2)^9\, u}{[(3/2)^2 - u]^5}\exp\left\{\frac{-3u}{(3/2)^2 - u}\right\}; \quad u \leqslant \frac{9}{4}. \tag{B5}$$

Equations (7) and (B5) predict maximum allowable particle sizes for MDC and IRC coarsening; they are $u_{max} = \frac{3}{2}$ for MDC coarsening and $u_{max} = (\frac{3}{2})^2 = \frac{9}{4}$ for IRC coarsening.

In the statistics community, measures of goodness of fit of theoretical distributions are nearly universally done by comparing theoretical CDFs with ECDFs [95]. In terms of the variable u, the CDF expresses the probability that a given particle has a scaled radius smaller than u; in mathematical terms, this is written as the equation

$$G(u) = \int_0^u g(x)dx, \tag{B6}$$

where $G(u)$ is the theoretical CDF. Since the theoretical PSDs are calculated using the variable z, it is necessary to take some care in comparing a theoretical CDF with an ECDF. It was shown [81] that $H(z)$, the theoretical CDF, satisfies the equality $H(z) = G(u)$, but since the statistical data in coarsening are expressed in terms of the variable u, and the CDF must be calculated using the variable z, it is necessary to transform z to u when analyzing experimental data. The general expression for $H(z)$ is [81]

$$H(z) = 1 - \exp[-\phi(z)]. \tag{B7}$$

Once $H(z)$ is calculated, u cannot simply be substituted for z for comparison with an ECDF. Instead, it is imperative to substitute $u = z/\langle z\rangle$, as is also done for the PSD.

2. Extraction and evaluation of data

It is customary in the phase-transformations community to report scaled PSDs in the form of histograms, which must satisfy four conditions, two of which have already been stated: (1) the area under the histogram A must equal unity and (2) the average value of u, $\langle u\rangle$, must also equal unity. Additionally, there are two other important criteria: (3) the width of every interval (bin) in a histogram must have the same value Δ and (4) the first bin in all histograms must begin at $u_k = 0$, where u_k represents the maximum value of u in the kth bin, and

$$u_{k+1} - u_k = \Delta. \tag{B8}$$

It is quite easy to take these requirements for granted, but if any one of them is not fulfilled, an accurate analysis cannot proceed. Assuming that all the frequencies in a histogram have been measured accurately, we note that, as a general observation, $A = 1$ will be satisfied provided that Δ accurately represents the width of the intervals in the histogram; condition (4) need not be satisfied because A is the same, no matter where the true origin $u_k = 0$ is located. However, condition (4) must be satisfied to calculate all higher moments of the PSD, including $\langle u\rangle$. This also holds for calculating the ECDF.

Within a histogram, the value of $g(u)$ is constant in each bin, and we designate it as g_k for the kth bin. It is easy to show that A and $\langle u\rangle$ are given by the equations

$$A = \Delta \sum_{k=1}^{N_h} g_k, \tag{B9}$$

and

$$\langle u\rangle = \Delta \sum_{k=1}^{N_h} u_k g_k - \frac{\Delta^2}{2} \sum_{k=1}^{N_h} g_k, \tag{B10}$$

for a histogram with N_h bins. A simpler formula for $\langle u\rangle$ is obtained on defining u_j in the center of the mth bin such that $u_j = u_k - \Delta/2$. Noting that $g_j = g_k$, $\langle u\rangle$ is given by the formula

$$\langle u\rangle = \Delta \sum_{j=1}^{N_h} u_j g_j. \tag{B11}$$

The ECDF, designated here as G_k, is readily computed using the formula

$$G_k = \Delta(G_{k-1} + g_k);\ G_0 = 0. \tag{B12}$$

3. Implementation of the statistical tests

In the limit of large N, the distribution of the quantity $K = \sqrt{N} D_N$ converges to the Kolmogorov distribution, which has the following CDF:

$$\Pr(x) = \frac{\sqrt{2\pi}}{x} \sum_{i=1}^{\infty} \exp\left[-\frac{(2i-1)^2\pi^2}{8x^2}\right] = \frac{1}{x}\sqrt{\frac{\pi}{2}}\vartheta_2\left[0, \exp\left(-\frac{\pi^2}{2x^2}\right)\right], \tag{B13}$$

where $\vartheta_i(z, q)$ is the Jacobi θ function (z and q are generic arguments used in this function). Equation (B13) expresses the probability that a randomly drawn sample from a given assumed theoretical distribution will have $K < x$. The p value is given by $p = 1\text{–}\Pr(x)$, and a small p value indicates that it is unlikely that the data came from the distribution $g(u)$. It is remarkable that the limiting distribution of the test statistic D_N does not depend on the theoretical $g(u)$. For finite samples, when N is on the order of hundreds, such as in typical coarsening experiments, the errors caused by using the $N \to \infty$ limit can reach a few percent. A simple fix is to substitute

$$x = \sqrt{N} D_N + \frac{1}{6\sqrt{N}} + \frac{\sqrt{N} D_N - 1}{N}, \tag{B14}$$

when evaluating the p value, which reduces the error to a fraction of a tenth of a percent when $N = 100$ [96].

The use of histograms in lieu of the raw data for N individual particles and the presence of a fitted PSD parameter n render the standard K-S test invalid, so Eq. (B13) cannot be used; to obtain a p value, one must resort to Monte Carlo simulations. The procedure we used to arrive at the best fit to the ECDFs involved two steps, the aim of which was to determine the optimum value of n and n_{opt} for each volume fraction.

The first step was a calculation of n_{opt} using the equation

$$n_{\text{opt}} = \arg\min_n D_N, \tag{B15}$$

which minimizes the maximum deviation between the ECDF and theoretical CDF of the TIDC theory. In practice, Eq. (B15) is discretized, and D_N is no longer evaluated using the supremum, Eq. (11), but by the approximation

$$D_N \approx \max_k |G_N(u_k) - G(u_k)|, \tag{B16}$$

where u_k is the maximum value of u in the kth bin, as in Eqs. (B9), (B10), and (B12). Some care must be exercised when minimizing Eq. (B16) numerically since the objective function is only piecewise differentiable. Since D_N in this case was evaluated using the ECDFs, we designate it as D_N^{ECDF}.

The next step involved Monte Carlo simulations to generate 10^5 random sets of size N_h drawn from the theoretical PSD, with N_h equaling the number of particles measured experimentally. Each set was converted into a histogram using the same bin widths and bin offsets as in the original ECDF. The simulations produced new values of n_{opt}, which were also

determined using Eq. (B15), as well as the new test statistic D_N^{MC}, which was also calculated using Eq. (B16) but with the values of $G(u_k)$ generated by the Monte Carlo simulations. Finally, the p values were estimated as the fraction of sets satisfying $D_N^{\mathrm{MC}} > D_N^{\mathrm{ECDF}}$. Uncertainty in the value of n_{opt} was estimated by taking the standard deviation of the fitted values over all 10^5 random sets. The results are presented in Table IV.

[1] I. M. Lifshitz and V. V. Slyozov, J. Phys. Chem. Solids **19**, 35 (1961).
[2] C. Wagner, Z. für Elektrochem. **65**, 581 (1961).
[3] A. J. Ardell, Mater. Sci. Eng. A **238**, 108 (1997).
[4] A. J. Ardell, J. Mater. Sci. **55**, 14588 (2020).
[5] A. J. Ardell, in *Phase transformations '87*, edited by G. W. Lorimer (University of Manchester, Manchester, UK, 1988), p. 485.
[6] P. W. Voorhees, Annu. Rev. Mater. Sci. **22**, 197 (1992).
[7] C. S. Jayanth and P. Nash, J. Mater. Sci. **24**, 3041 (1989).
[8] A. Baldan, J. Mater. Sci. **37**, 2171 (2002).
[9] K. G. Wang, M. E. Glicksman, and K. Rajan, Comput. Mater. Sci. **34**, 235 (2005).
[10] P. E. Di Nunzio, Philos. Mag. **98**, 1674 (2018).
[11] D. V. Alexandrov, Philos. Mag. Lett. **96**, 355 (2016).
[12] J. D. Livingston, Trans. Am. Inst. Min. Metall. Eng. **215**, 566 (1959).
[13] A. J. Ardell and R. B. Nicholson, J. Phys. Chem. Solids **27**, 1793 (1966).
[14] K. Mahalingam, B. P. Gu, G. L. Liedl, and T. H. Sanders, Acta Metall. **35**, 483 (1987).
[15] A. J. Ardell and R. B. Nicholson, Acta Metall. **14**, 1295 (1966).
[16] D. J. Chellman and A. J. Ardell, Acta Metall. **22**, 577 (1974).
[17] J. Wimmel and A. J. Ardell, J. Alloys Compd. **205**, 215 (1994).
[18] D. Kim and A. J. Ardell, Metall. Mater. Trans. A **35**, 3063 (2004).
[19] J. Wimmel and A. J. Ardell, Mater. Sci. Eng. A **183**, 169 (1994).
[20] D. Kim and A. J. Ardell, Acta Mater. **51**, 4073 (2003).
[21] M. Meshkinpour and A. J. Ardell, Mater. Sci. Eng. A **185**, 153 (1994).
[22] J.-H. Cho and A. J. Ardell, Acta Mater. **45**, 1393 (1997).
[23] J.-H. Cho and A. J. Ardell, Acta Mater. **46**, 5907 (1998).
[24] D. Kim and A. J. Ardell, Scr. Mater. **43**, 381 (2000).
[25] A. J. Ardell, D. Kim, and V. Ozolins, Z. Metallkd. **97**, 295 (2006).
[26] A. Maheshwari and A. J. Ardell, Acta Metall. Mater. **40**, 2661 (1992).
[27] A. J. Ardell and V. Ozolins, Nat. Mater. **4**, 309 (2005).
[28] Y. Mishin, Acta Mater. **52**, 1451 (2004).
[29] M. M. P. Janssen, Metall. Trans. **4**, 1623 (1973).
[30] K. Fujiwara and Z. Horita, Acta Mater. **50**, 1571 (2002).
[31] A. J. Ardell, Acta Mater. **58**, 4325 (2010).
[32] A. J. Ardell, Philos. Mag. **94**, 2101 (2014).
[33] C. H. Kang and D. N. Yoon, Metall. Trans. A **12**, 65 (1981).
[34] W. Bender and L. Ratke, Acta Mater. **46**, 1125 (1998).
[35] I. Seyhan, L. Ratke, W. Bender, and P. W. Voorhees, Metall. Mater. Trans. A **27**, 2470 (1996).
[36] D. J. Rowenhorst, J. Alkemper, V. Snyder, and P. W. Voorhees, in *Conference and Exhibit on International Space Station Utilization* (AIAA, Cape Canaveral, 2001).
[37] D. Kammer, A. Genau, P. W. Voorhees, W. M. Duval, R. W. Hawersaat, J. M. Hickman, T. Lorik, D. G. Hall, and C. A. Frey, in *47th AIAA Aerospace Sciences Meeting Including the New Horizons Forum and Aerospace Exhibition* (AIAA, Cape Canaveral, 2009).
[38] W. M. B. Duval, R. W. Hawersaat, T. Lorik, J. Thompson, B. Gulsoy, and P. W. Voorhees, in *Materials Science and Technology (MS&T) 2013* (Montreal, Quebec, Canada, 2013), https://ntrs.nasa.gov/search.jsp?R=20140009204.
[39] J. D. Thompson, E. B. Gulsoy, and P. W. Voorhees, Acta Mater. **100**, 282 (2015).
[40] T. L. Ngai and Y. A. Chang, Calphad **5**, 267 (1981).
[41] J. Alkemper and P. W. Voorhees, J. Microsc. **201**, 388 (2001).
[42] D. Kammer and P. W. Voorhees, MRS Bull. **33**, 603 (2008).
[43] C. K. L. Davies, P. Nash, and R. N. Stevens, Acta Metall. **28**, 179 (1980).
[44] V. A. Snyder, J. Alkemper, and P. W. Voorhees, Acta Mater. **48**, 2689 (2000).
[45] V. A. Snyder, J. Alkemper, and P. W. Voorhees, Acta Mater. **49**, 699 (2001).
[46] D. J. Rowenhorst, J. P. Kuang, K. Thornton, and P. W. Voorhees, Acta Mater. **54**, 2027 (2006).
[47] S. C. Hardy, G. B. McFadden, S. R. Coriell, P. W. Voorhees, and R. F. Sekerka, J. Cryst. Growth **114**, 467 (1991).
[48] D. J. Rowenhorst and P. W. Voorhees, Annu. Rev. Mater. Res. **42**, 105 (2012).
[49] E. B. Gulsoy, K. Wittman, J. Thompson, and P. W. Voorhees, in *49th AIAA Aerospace Sciences Meeting Including the New Horizons Forum and Aerospace Exhibition* (AIAA, Orlando, 2011).
[50] J. D. Thompson, Coarsening in solid liquid systems: A verification of fundamental theory, Ph.D. Thesis, Northwestern University, 2015.
[51] J. Alkemper, V. A. Snyder, N. Akaiwa, and P. W. Voorhees, Phys. Rev. Lett. **82**, 2725 (1999).
[52] V. A. Snyder, N. Akaiwa, J. Alkemper, and P. W. Voorhees, Metall. Mater. Trans. A **30**, 2341 (1999).
[53] N. Akaiwa and P. W. Voorhees, Phys. Rev. E **49**, 3860 (1994).
[54] M. Zinke-Allmang, L. C. Feldman, and M. H. Grabow, Surf. Sci. Rep. **16**, 377 (1992).
[55] N. T. K. Thanh, N. Maclean, and S. Mahiddine, Chem. Rev. **114**, 7610 (2014).
[56] K. C. Lai, Y. Han, P. Spurgeon, W. Huang, P. A. Thiel, D. J. Liu, and J. W. Evans, Chem. Rev. **119**, 6670 (2019).
[57] A. J. Ardell, Acta Mater. **61**, 7828 (2013).
[58] Y. Ma and A. J. Ardell, Acta Mater. **55**, 4419 (2007).
[59] A. J. Ardell and Y. Ma, Mater. Sci. Eng. A **550**, 66 (2012).
[60] C. A. Becker, M. Asta, J. J. Hoyt, and S. M. Foiles, J. Chem. Phys. **124**, 164708 (2006).
[61] D. Buta, M. Asta, and J. J. Hoyt, Phys. Rev. E **78**, 031605 (2008).
[62] C. A. Becker, D. L. Olmsted, M. Asta, J. J. Hoyt, and S. M. Foiles, Phys. Rev. B **79**, 054109 (2009).
[63] T. Frolov and Y. Mishin, J. Chem. Phys. **131**, 054702 (2009).

[64] Y. Yang, H. Humadi, D. Buta, B. B. Laird, D. Sun, J. J. Hoyt, and M. Asta, Phys. Rev. Lett. **107**, 025505 (2011).
[65] E. Asadi, M. A. Zaeem, S. Nouranian, and M. I. Baskes, Acta Mater. **86**, 169 (2015).
[66] J. P. Palafox-Hernandez and B. B. Laird, J. Chem. Phys. **145**, 211914 (2016).
[67] C. Qi, B. Xu, L. T. Kong, and J. F. Li, J. Alloys Compd. **708**, 1073 (2017).
[68] J. J. Hoyt, S. Raman, N. Ma, and M. Asta, Comput. Mater. Sci. **154**, 303 (2018).
[69] H. Liang, B. B. Laird, M. Asta, and Y. Yang, Acta Mater. **143**, 329 (2018).
[70] C. Xu, X. Meng, X. Sun, X. Gan, P. Li, S. Xiao, H. Deng, X. Li, and W. Hu, J. Alloys Compd. **763**, 1 (2018).
[71] S. A. Etesami, M. I. Baskes, M. Laradji, and E. Asadi, Acta Mater. **161**, 320 (2018).
[72] S. Plimpton, J. Comput. Phys. **117**, 1 (1995).
[73] J. Crank, *The Mathematics of Diffusion*, 2nd ed. (Oxford University Press, London, UK, 1975), p. 273.
[74] R. A. Khairulin, S. V. Stankus, and A. S. Kosheleva, High Temp. **46**, 212 (2008).
[75] J. Cahoon, Y. Jiao, K. Tandon, and M. Chaturvedi, Journal of Phase Equilibria and Diffusion **27**, 325 (2006).
[76] J. D. Meakin and E. Klokholm, Trans. Am. Inst. Min. Metall. Eng. **218**, 463 (1960).
[77] C. Coston and N. H. Nachtrieb, J. Phys. Chem. **68**, 2219 (1964).
[78] F. H. Huang and H. B. Huntington, Phys. Rev. B **9**, 1479 (1974).
[79] R. M. Jordan and J. D. Hunt, Metall. Trans. **2**, 3401 (1971).
[80] F. J. Massey, J. Am. Stat. Assoc. **46**, 68 (1951).
[81] A. J. Ardell, Metallography **5**, 285 (1972).
[82] A. J. Ardell, J. Mater. Sci. **51**, 6133 (2016).
[83] S. P. Marsh and M. E. Glicksman, Acta Mater. **44**, 3761 (1996).
[84] A. D. Brailsford and P. Wynblatt, Acta Metall. **27**, 489 (1979).
[85] W. Bender and L. Ratke, Scr. Metall. Mater. **28**, 737 (1993).
[86] B. Sadigh, P. Erhart, A. Stukowski, E Martinez A.Caro, and L. Zepeda-Ruiz, Phys. Rev. B **85**, 184203 (2012).
[87] J. R. Morris and X. Y. Song, J. Chem. Phys. **116**, 9352 (2002).
[88] P. L. Williams, Y. Mishin, and J. C. Hamilton, Model. Simul. Mater. Sci. Eng. **14**, 817 (2006).
[89] G. P. P. Pun and Y. Mishin, Philos. Mag. **89**, 3245 (2009).
[90] A. Stukowski, Model. Simul. Mater. Sci. Eng. **18**, 015012 (2010).
[91] J. Hickman and Y. Mishin, Phys. Rev. B **93**, 224108 (2016).
[92] C. A. Howells and Y. Mishin, Simul. Mater. Sci. Eng. **26**, 085008 (2018).
[93] P. J. Steinhardt, D. R. Nelson, and M. Ronchetti, Phys. Rev. B **28**, 784 (1983).
[94] M. Hillert, Acta Metall. **13**, 227 (1965).
[95] M. A. Stephens, J. Am. Stat. Assoc. **69**, 730 (1974).
[96] J. Vrbik, Pioneer J. Theor. Appl. Stat. **15**, 15 (2018).